Microstructural study of the NbC to G-phase transformation in HP-Nb alloys

Nicolas Vaché, Philippe Steyer, C. Duret-Thual, M. Perez, Thierry Douillard, E. Rauch, M. Véron, G. Renou, F. Dupoiron, C. Augustin, et al.

To cite this version:

Nicolas Vaché, Philippe Steyer, C. Duret-Thual, M. Perez, Thierry Douillard, et al.. Microstructural study of the NbC to G-phase transformation in HP-Nb alloys. Materialia, 2020, 9, pp.100593. 10.1016/j.mtla.2020.100593 . hal-02504312

HAL Id: hal-02504312

https://hal.science/hal-02504312

Submitted on 21 Jul 2022

Microstructural study of the NbC to G-phase transformation in HP-Nb alloys.

N. Vaché[1,3], P. Steyer[1], C. Duret-Thual[1,2], M. Perez[1], T. Douillard[1], E. Rauch[4], M. Véron[4], G. Renou[4], F. Dupoiron[3], C. Augustin[3] and S. Cazottes[1*]

[1] Univ. Lyon, INSA-Lyon, MATEIS UMR CNRS 5510, 7 avenue Jean Capelle, 69621 Villeurbanne, France

[2]French Corrosion Institute, ZA du parc secteur Gampille F-42490 Fraisses, France

[3] Total TRTG (Total Recherche et Technologie de Gonfreville), BP 27 76700 Harfleur, France

[4]Univ. Grenoble Alpes, CNRS, Grenoble INP, SIMAP, 38000 Grenoble, France

*Corresponding author: sophie.cazottes@insa-lyon.fr

Abstract

The microstructure of a centrifugally cast HP alloy was studied in its as-received state and after ageing at 900 °C. A multi-scale approach combining X Ray Diffraction (XRD), advanced electron microscopy modes (scanning and transmission electron microscopies (SEM, TEM), together with focused ion beam / SEM nanotomography (FIB-nt)) has been carried out to characterize the evolution of niobium carbides during ageing. After thermal treatment, the carbides exhibit a complex microstructure, consisting of a core of untransformed NbC, an intermediate layer of G-phase ($Ni_{16}Nb_6Si_7$) with embedded nanometric titanium carbide precipitates, and an outer shell of alternating chromium carbides $Cr_{23}C_6$ and G-phase. A simple diffusion model was used to explain the faster external growth of G-phase compared to the internal NbC dissolution, and to determine a diffusion coefficient of niobium in the G-phase at 900 °C.

Keywords HP-Nb alloy; microstructure; ageing; G-phase; NbC; advanced material characterization

1. Introduction

Heat resistant High Performance (HP)-Nb alloys are commonly used in both chemical and energy industries owing to their low chemical reactivity combined to good mechanical properties at high temperatures. HP-Nb alloys are fully austenitic steels with a high amount of nickel (~35 wt%), and chromium (~25 wt%). Alloying elements such as niobium, titanium and zirconium are added to form the carbides network on the basis of their excellent mechanical properties (Andrade et al., 2015). A Thermo-Calc simulation of this type of alloy using the TCFE8 database is presented in Figure 1.

In its as cast state, HP alloys microstructure consists of a nickel and chromium-rich austenitic matrix associated with an interdendritic network of chromium and niobium-rich carbides (M_7C_3 and NbC respectively). For sake of clarity, M_7C_3 (and later on $M_{23}C_6$) will be referred as Cr_7C_3 ($Cr_{23}C_6$ respectively) in the following. Titanium is also added to the alloy to stabilize the niobium carbides, and to refine the interdendritic carbide network (Sustaita-Torres et al., 2012a). Buchanan have shown that the 3D morphology of NbC consists of a Ti(Al)-rich core inclusion with elongated branches around it (Buchanan et al., 2014a). Therefore, a composition gradient of titanium is found within the NbC precipitate: from 5 wt.% Ti near the vicinity of the core and decreasing along the branches.

A high temperature exposure of the as-cast state leads to a primary carbide transformation of Cr_7C_3 into $Cr_{23}C_6$, and a secondary precipitation of $Cr_{23}C_6$ in the matrix. For heat treatments below 920 °C NbC transforms into a nickel niobium silicide called G-phase, known for its detrimental effect on the mechanical properties (Guo et al., 2017; Shi et al., 2008). According to the Thermo-Calc simulation a complete dissolution of the NbC is expected for temperatures lower than 750 °C but the Time-Temperature-Precipitation diagram of the 20Cr25Ni alloy, proposed by Powell *et al.* (Powell et al., 1988), indicates a residual presence of NbC after several thousand hours of ageing at 850 °C. The composition of G-phase varies from Ni_3Nb_2Si (Buscail et al., 2017; Sustaita-Torres et al., 2012b) to $Ni_{16}Nb_6Si_7$ (Barbabela et al., 1991c; Berghof-Hasselbächer et al.; de Almeida Soares et al., 1992b; Ecob et al., 1987b; Ibañez et al., 1999b; Mateo et al., 1997; Sustaita-Torres et al., 2012b). In titanium-containing HP alloys, the transformation of NbC into G-phase is accompanied by the formation of nanometric titanium-rich precipitates, characterized by Almeida *et al.* as TiC (de Almeida et al., 2003a). They conclude that the dissolution of NbC precipitates is controlled by the amount of Ti initially present in the NbCs, and that the addition of Ti in the composition lead to a smaller amount of G-phase, which is beneficial for mechanical properties. (Buchanan et al., 2014a). The silicon is another critical alloying element for HP alloys. A study by Dewar *et al.* (Dewar and Gerlich, 2013), combining thermodynamic calculations (performed on the Thermo-Calc software) and experimental measurements, has highlighted the predominant role of silicon and nitrogen elements over the transformation kinetics and stability domains of NbC. Experimentally, Almeida (Pedro Ibañez et al., 1993) has also stated that increasing the amount of Si in the alloy increases the kinetic of the NbC to G-phase transformation. Indeed, Thermo-Calc simulations performed in the present work for two Si content (2.50 wt% and 1.65wt%) reveal that an increase in Si content shifts the NbC/G-phase transformation to high temperatures (Figure 1c).

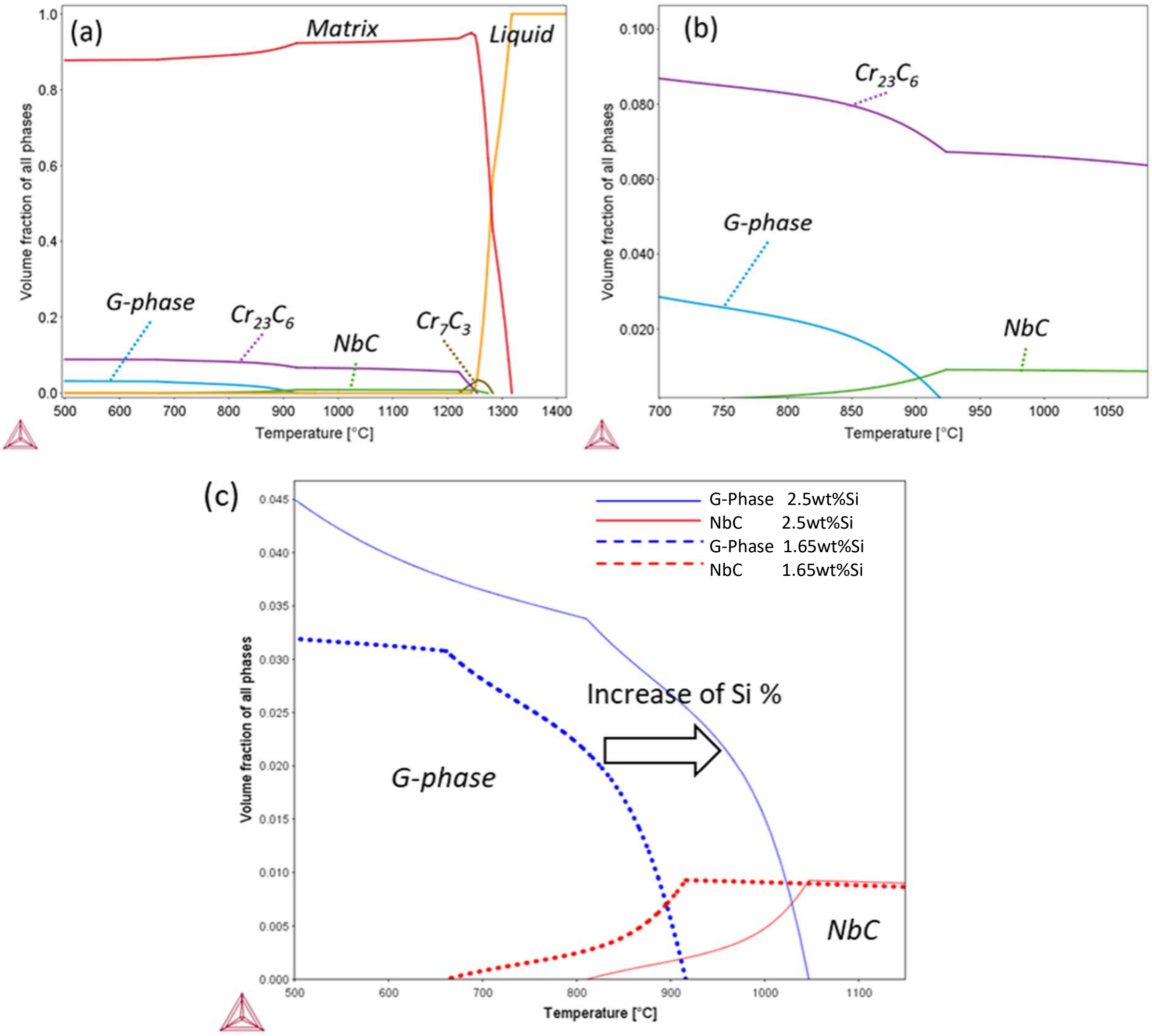

Figure 1: (a) Volume fraction of phase as a function of temperature calculated from Thermo-Calc software, using the TCFE8 database and HP alloy composition (table 1). (b) Enlargement of the 700-1100 °C domain for which the NbC→G-phase transformation takes place. (c) Evolution of the stability domains of the NbC and phase-G phases for two silicon contents.

If the consequences of the G-phase formation for many Nb-containing NiCr alloys on the mechanical properties is well-known, the precise mechanism and kinetics of NbC to G-phase transformation is not well documented. The objective of this paper is to accurately characterize the microstructure of the niobium carbides present in the HP-Nb alloy after ageing at 900°C. A multi-scale approach is adopted, combining information from a global to local analyses, and surface (SEM) to volume (TEM, FIB) characterizations.

2. Experimental

The studied material is a commercial HP-Nb cast alloy whose standard composition is described in ASTM A297. A nominal composition of the alloy is given in table 1. In the rest of this document the chemical composition of the matrix will be given in wt.% (as conventionally used) and the composition of carbides and G-phase in at.% (in order to evoke their chemical formula). Thermal ageing tests were performed in a tubular furnace for 24 h and 100 h at 900 °C under secondary vacuum (10^{-6} mbar).

XRD surface characterizations of as-cast and aged samples were carried out using a Brucker D8 Advanced diffractometer with a copper anticathode ($CuK\alpha_1$ = 1.5406 Å). Operating conditions were 2θ scan, 0.02° step size ranging from 30° to 60°, 8 s counting time for a voltage and current of 40 kV and 40 mA, respectively. XRD measurements were performed on bulk samples, and also on powder after dissolution of the matrix, using the Berzelius reagent (1.85 liters H_20, 320 g cupric chloride, 280 g potassium chloride, 1.5 ml hydrochloric acid, 20 g of tartaric acid (Burke, 1975)).

Table 1 : Chemical composition of the studied alloy (wt.%)

C	Ni	Cr	Mn	Si	Nb	Ti	Fe
0.4-0.5	32-36	25-27	1.3-1.5	1.5-1.8	0.6-0.8	0.05-0.07	Bal.

Various surface treatments and observation conditions in the scanning electron microscope (SEM) were chosen depending on the observation goals. For general microstructure examinations and XRD analyses, samples were ground with SiC paper from P400 to P1200 grades, then 3 µm-polished with diamond spray, ultrasonically cleaned in an ethanol-water mixture and rinsed in deionized water. For a deeper SEM characterization of as-cast NbC microstructure, HP-Nb sample was etched 1 minute in Berzelius solution at room temperature. Both SEM observations and EDX mapping were performed using a field-emission scanning electron microscope (FESEM Zeiss SUPRA 55VP) under 10 kV accelerating voltage. In order to observe the NbC/G-phase fine microstructure after ageing, an ionic (Ar^+) polishing was carried out using an Ilion+ GATAN model-697. SEM characterizations were then conducted at low accelerating voltage (2 kV) using a secondary electrons (SE) in-lens detector.

The composition measurements and X-ray mapping were carried out by using an energy-dispersive X-ray system (EDXS) with an X-max 80 mm² Silicon Drift Detector (Oxford Instruments, Abingdon, Oxfordshire, UK). At the TEM scale, orientation maps of aged NbC/G-phase precipitates were acquired with the ASTAR system from NanoMEGAS SPRL (Brussels). With this TEM attachment, the electron beam is scanned over the area of interest and the successive diffraction patterns are recorded with an optical camera and memorized. Phase and/or orientation maps are reconstructed by indexing the patterns with a dedicated template matching algorithm(E.F. Rauch and Véron, 2014). ASTAR acquisitions were performed on a field-emission transmission electron microscope at 200kV (JEOL 2100F). Virtual Dark Field images are reconstructed from any selected diffraction pattern. This allows an enhanced analysis of minority phases (Portillo et al., 2010). The crystallographic data of the different phases are listed in Table 2.

Table 2: List of crystallographic structures.

	Space group	Lattice parameter (nm)	Atomic positions
M_7C_3	$Pnma$	a=0.450 b=0.694 c=1.203	Cr1(0.25;0.07;0.02) Cr2(0;0.07;0.81) Cr3(0.24;0.25;0.2) Cr4(0.25;0.25;0.42) Cr5(0;0.25;0.61) C1(0.11;0.03;0.35) C2(0.38;0.25;0.57)
NbC	$Fm\bar{3}m$	a=0.447	C(0.5;0.5;0.5) Nb(0;0;0)
$M_{23}C_6$	$Fm\bar{3}m$	a=1.063	Cr(0;0.17;0.17) C(0.275;0;0)
G phase ($Ni_{16}Nb_6Si_7$)	$Fm\bar{3}m$	a=1.12	Si1(0;0;0) Si2(0;0.25;0.25) Nb(0.3;0;0) Ni1(1/3;1/3;1/3) Ni2(0.118;0.118;0.118)
TiC	$Fm\bar{3}m$	a=0.4319	C(0.5;0.5;0.5) Ti(0;0;0)
Matrix (γ)	$Fm\bar{3}m$	a=0.36	Fe(0;0;0)

3D images realized by FIB / SEM tomography give access to additional volumic key-information. Serial FIB/SEM imaging was performed using a FIB/SEM workstation (NVision 40; Carl Zeiss Microscopy GmbH, Oberkochen, Germany) combining a SIINT zeta FIB column (Seiko Instruments Inc. NanoTechnology, Japan) with a Gemini I SEM column. The principle of

FIB tomography is based on a stacking of 2D images, obtained by performing serial FIB sectioning and SEM imaging, to reconstruct the microstructure in the three dimensions. The adapted procedure is more detailed in (Baulin et al., 2019). The pixel size was set to 10 nm in *x*, *y* and *z* directions. Serial FIB sectioning was done with a current of 700 pA at 30 kV.

3. Results

3.1 As-cast alloy

M_7C_3 and MC precipitates are present in the austenitic matrix (Figure 2a). In M_7C_3 carbides, the metallic element stands for Fe (7%) and Cr (69%), and will be called Cr_7C_3 in the following part of the text. In MC carbides, 6at% Ti was found, the rest of the metallic element being Nb, therefore, this carbide will be called NbC latter in the text. The Table 3 presents the composition of the NbC, the large Cr_7C_3 and the matrix. Niobium carbides are also surrounded by fine Cr_7C_3 precipitates (Figure 2b), as already observed by (Sustaita-Torres et al., 2012b) and by Buchanan et al (Buchanan et al., 2014b). The formation mechanism of those Cr_7C_3 remains undescribed. The chemistry of the matrix is affected by the presence of NbC precipitates. In particular, the silicon content, which averages 1.3wt.% in the austenitic matrix, gradually increases over a distance of a few microns to reach 2.0wt% in contact with NbC (Figure 2c and d). This segregation can be explained by the release of the alloying elements in the interdendritic region during the alloy solidification. Si is known to influence kinetics of the NbC into G-phase transformation, and the effect of this interfacial segregation is discussed later in the text.

Table 3: composition of NbC, M_7C_3 and matrix of the as-cast alloy.

at.%	C	Si	Ti	Cr	Fe	Ni	Nb
NbC	40	1	6	4	1		48
M_7C_3	24	-	-	69	7	-	-
matrix	42	4		36	7	10	1

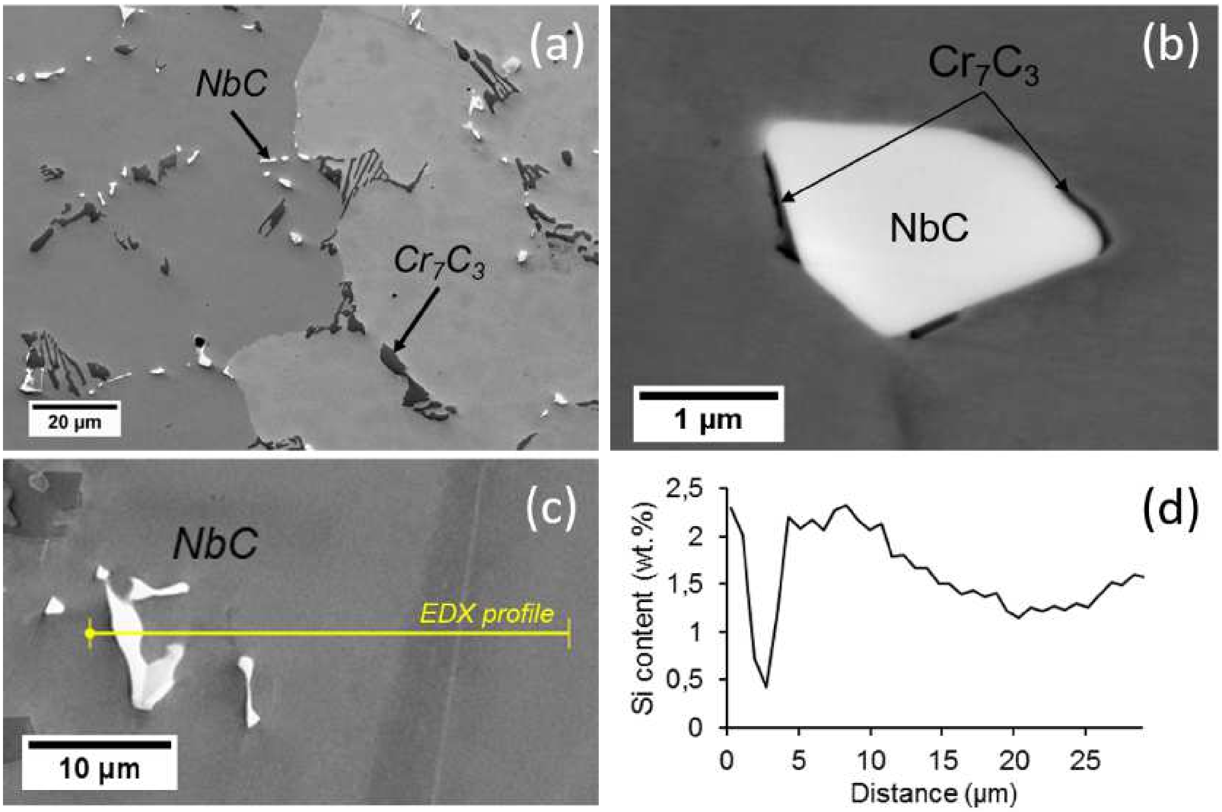

Figure 2: Microstructure of the as-cast alloy: (a) SEM observation in backscattered (BSE) mode showing the presence of NbC and Cr_7C_3 precipitates in the austenitic matrix, (b) SEM-BSE image of a niobium carbide surrounded by fine chromium carbide precipitates. The sample was etched 1min. using Berzelius solution, c) SEM-BSE image of NbC and d) corresponding EDX profile showing the Si content increase near the carbide.

3.2 Aged alloy

After 900 °C ageing for 24h, a secondary precipitation of $Cr_{23}C_6$ in the austenitic matrix is observed as well as the transformation of Cr_7C_3 precipitates into $Cr_{23}C_6$. Those two phenomena are well documented (Andrade et al., 2015; Barbabela et al., 1991; de Almeida et al., 2003a; de Almeida Soares et al., 1992; Ibañez et al., 1999; Kenik, 2003; Mostafaei et al., 2009; Nunes et al., 2007; Shi and Lippold, 2008; Sourmail, 2001) and will not be described here.

The nature of the phases formed during the NbC transformation into G-phase were investigated by TEM and SEM. ASTAR maps (Figure 3 (a) and (b)) reveal that the dissolution of the NbC is associated with the formation of G-phase and $Cr_{23}C_6$ carbides. An alternating pattern of those two phases is visible at the surface of the NbC. Orientation maps displayed in inverse pole figure (IPF) coloring (Figure 3 (c) and (d)) indicate that the $Cr_{23}C_6$ grow with a cube on cube orientation relationship (OR) within the matrix. This is expected, as the $Cr_{23}C_6$ is fcc like the matrix, and present a lattice parameter exactly three times higher than the one of the matrix (de Almeida et al., 2003a). At the contrary, no specific OR was found between the G-phase and the matrix, nor with the dissolving NbC.

Additionally, a similar area was analyzed by means of SEM – EDX mapping Figure 3 (e) and (f). The use of the in-lens detector improves the spatial resolution of the images, but modifies the contrast of the different observed phases. Both niobium and chromium carbides appear in dark, while the bright-contrasted phase, consisting of nickel, silicon and niobium (EDX maps), corresponds to the G-phase. The alternation of $Cr_{23}C_6$ and G-phase at the surrounding of the NbC is very clear on the SEM – In lens image. The composition of the different phases measured by EDX is presented in Table 4. Due to the low precision of the technique on light elements, the carbon content should be taken as an indication, however, the ratio between other elements remains correct. One can see that the NbC contains quite a large amount of Ti which is consistent with the study of Almeida *et al.* (de Almeida et al., 2003b). The chemical composition evolution across the different phases was measured through an EDX line scan (Figure 4). The concentration in Ni and Cr decreases almost linearly in the G-phase, from the matrix composition down to almost zero in the NbC. It reveals an enrichment of the Matrix in Si at the G-phase/matrix interface, while the Ti and Nb content increases to reach the values found in the NbC core. It indicates that the G-phase presents a composition gradient.

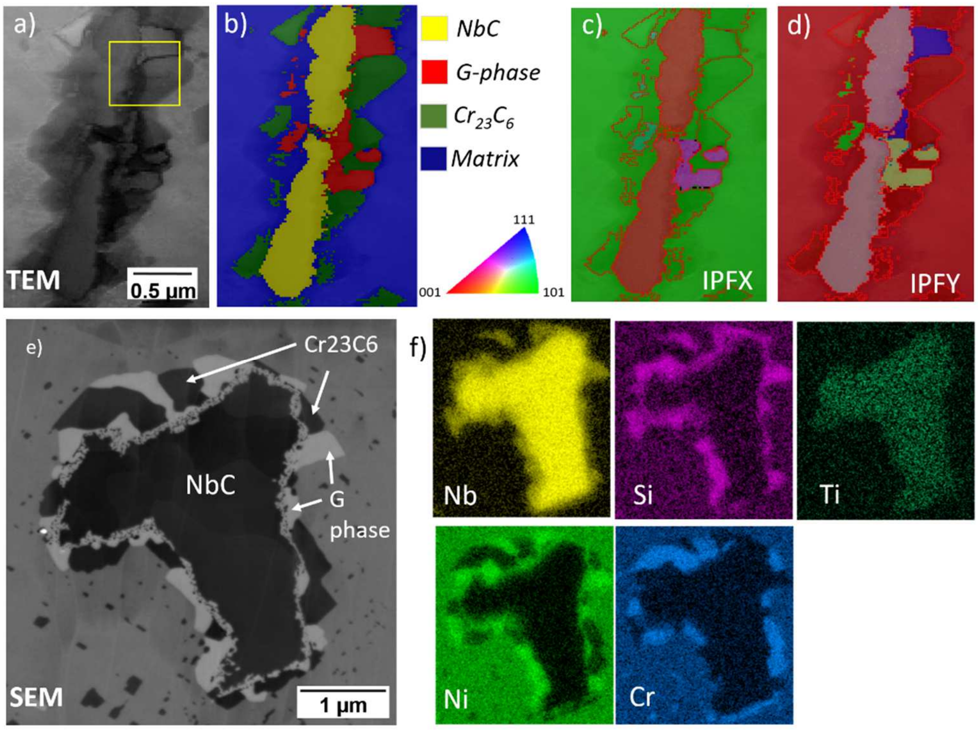

Figure 3: (a) to (d) ASTAR maps of a dissolving NbC after after 24 h of ageing at 900 °C (step size of 20 nm) (a) correlation index map , (b) phase distribution a(c) IPFX map, (d) IPFY map. The yellow square represents the second analyzed area involved in figure 5. (e) SEM-Inlens observation of a similar zone with (f) corresponding EDX maps (Nb, Si, Ti, Ni and Cr).

Table 4: EDX composition measurement of NbC, G-phase and $M_{23}C_6$ after ageing 24 h at 900 °C

at.%	C	Si	Ti	Cr	Fe	Ni	Nb
NbC	30	2	6	4	1		57
G-phase	11	23		7	6	37	16
$M_{23}C_6$	42	4		36	7	10	1

Higher magnification observations reveal that the NbC core is separated from the $M_{23}C_6$/G-phase peripheral zone by a thin intermediate layer of G-phase (Figure 5), located at the initial NbC/austenite interface. This spongy-like layer consisting of G-phase appears bright) and seems to be growing towards the center of the NbC. Dark nanoprecipitates (highlighted in yellow) are also present in this layer. As their diameter does not exceed 30nm, TEM was used to determine the nature and chemistry of the nanoparticles, see Figure 5b and c. The TEM – EDX profile reveals a Ti enrichment at the position of the precipitate.

The high amount of Ni, Nb and Si detected is attributed to the surrounding G-phase, located above or under the nano-precipitate in the thin foil. ASTAR maps were additionally used to validate the nature of those Ti-rich precipitates. A Virtual Bright Field (VBF) image of the NbC/G-phase interface can be created, as presented in Figure 5d. The contrasts observed here are similar to the one generated in Bright Field imaging in the conventional TEM imaging. Each contrast corresponds to a different orientation of the observed grains. Additionally, the 'Virtual DarkField' (VDF) mode of ASTAR has the capability of reproducing the characteristics of Dark Field Imaging in conventional TEM. The Virtual term stands for the fact that this procedure is entirely numerical and it presents a large flexibility in terms of shape and size of the aperture (Edgar F. Rauch and Véron, 2014). A VDF image (Figure 5e) of the interface was created by choosing an extra spot corresponding to the largest Nanoparticle identified, which is encircled in red in Figure 5d. Not only one but many precipitates appear white, as well as the adjacent NbC grain. Those nanoparticles and the NbC grain therefore share a common lattice plane. This demonstrates that the nanometric precipitates located in the G-phase interlayer present the same orientation, which is also the one of the dissolving NbC. Considering that TiC and NbC present a very similar lattice structure (Fm3m, a = 4.6 Å for TiC and a= 4.4 Å for NbC), it can be assumed that those nanoparticle are (Ti,Nb)C nanoparticles. This assumption is in agreement with the observations already reported by (de Almeida et al., 2003b). However, in their study, no particular OR between the dissolving NbC and the nanoparticles formed was reported.

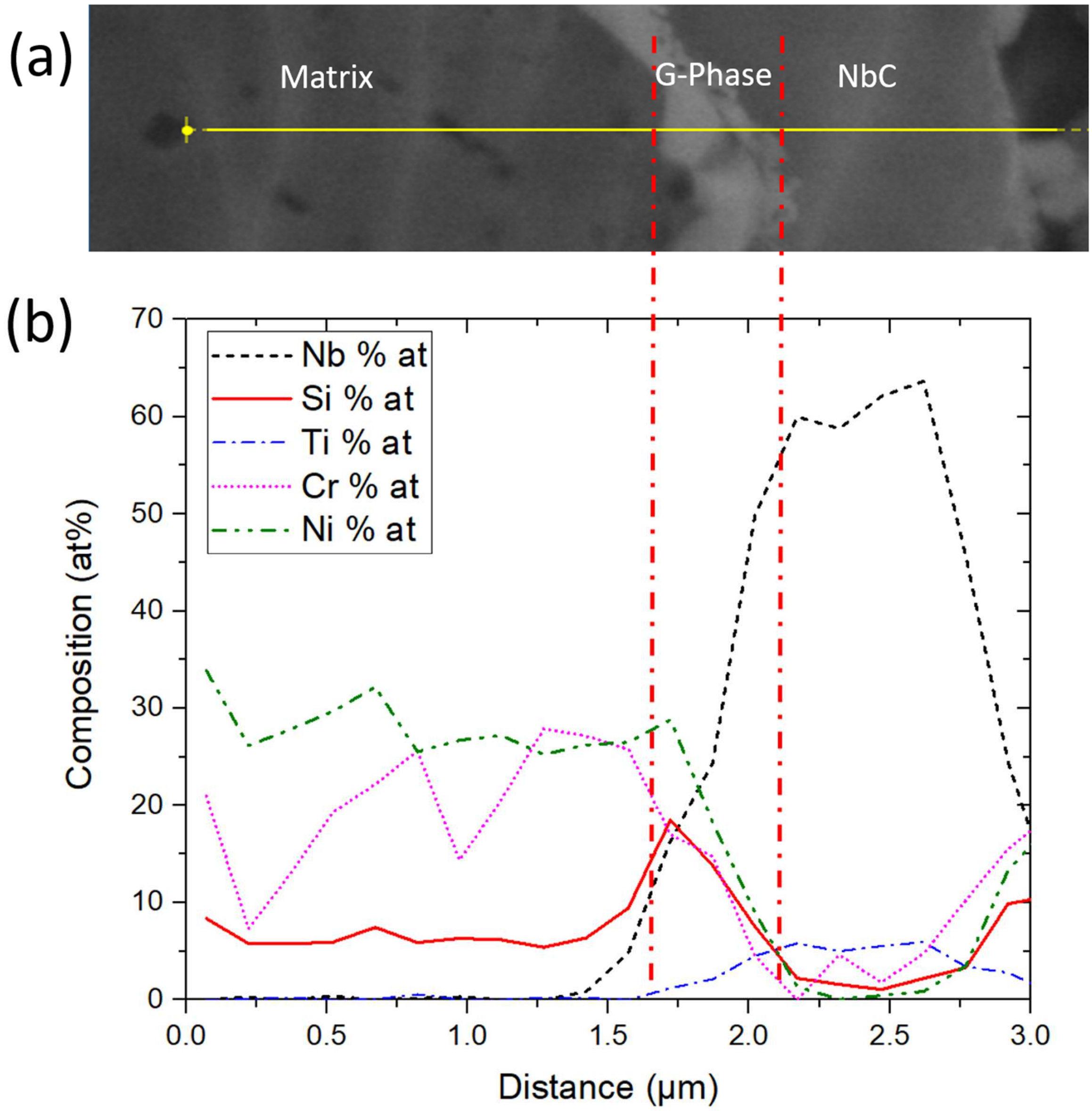

Figure 4: (a) SE-SEM image micrograph of a NbC after 24 h ageing at 900 °C, (b) SEM-EDX line scan across the different phases composing the partially transformed NbC.

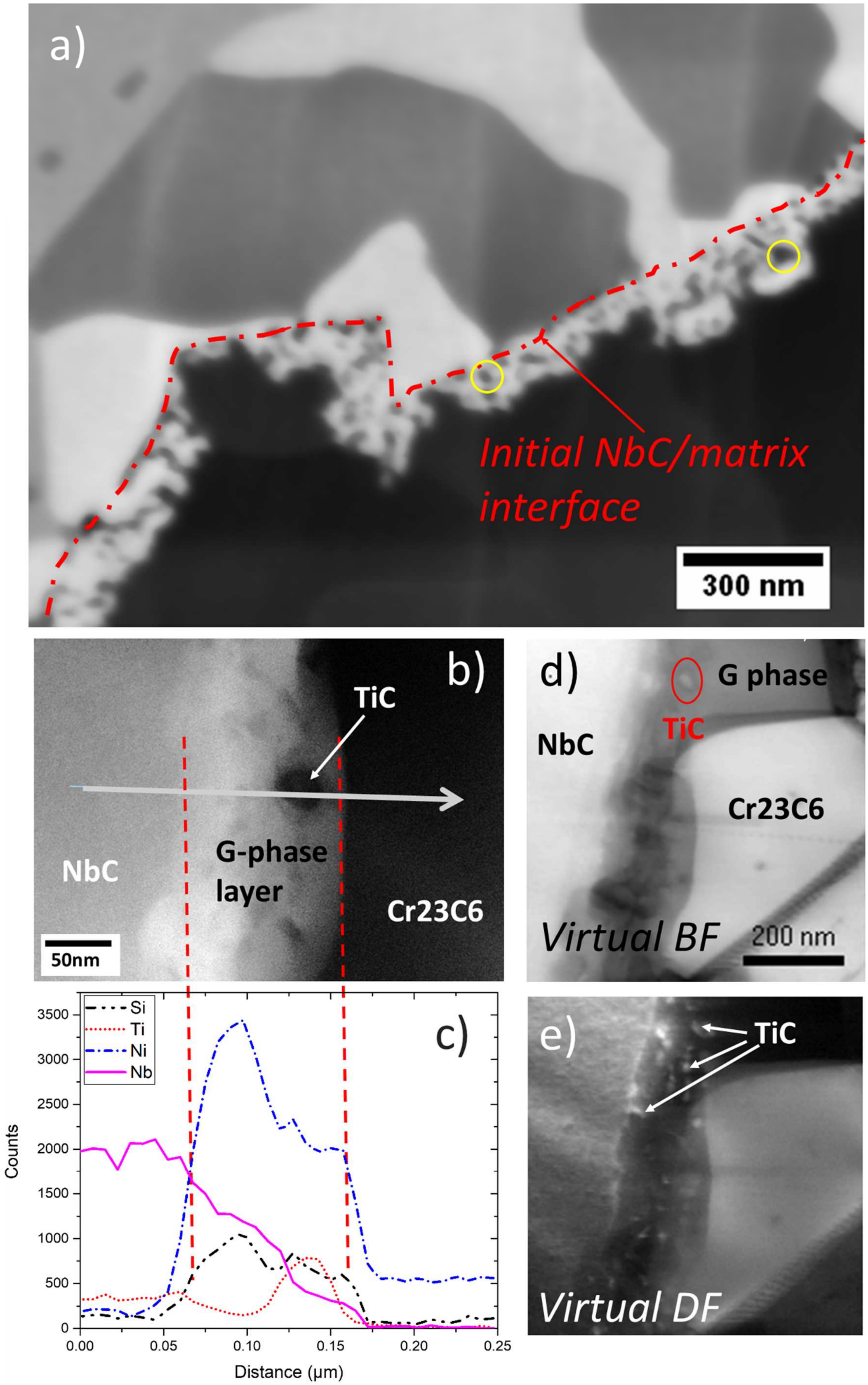
a)
Initial NbC/matrix interface
300 nm
b)
TiC
NbC
G-phase layer
Cr23C6
50nm
c)
Si
Ti
Ni
Nb
Counts
3500
3000
2500
2000
1500
1000
500
0
0.00
0.05
0.10
0.15
0.20
0.25
Distance (µm)
d)
G phase
TiC
NbC
Cr23C6
Virtual BF
200 nm
e)
TiC
Virtual DF

Figure 5: (a) SE-SEM image (in-lens) micrograph of a NbC after 24 h ageing at 900 °C. The initial interface between NbC and matrix is indicated as a red dashed line, and TiCs are encircled in yellow (b) TEM observation of a TiC nanoparticle located in the G-phase layer, and (c) corresponding TEM-EDX scan. (d) ASTAR Virtual Bright-Field of the surrounding area of a NbC (area represented as a yellow square on Figure 3a), and (c) Virtual Dark Field reconstruction highlighting the orientation relationship of the TiC with the dissolving NbC.

To better understand the transformation kinetics and the role of alloying elements, two ageing states, short and long, were characterized in 3D using the FIB-nanotomography: 24 and 100h at 900 °C. The reconstructed volumes are presented on Figure 6a and b. In both cases, the volumes are centered on a partially transformed NbC region. Images were recorded in SE (In lens) mode, with an accelerating voltage of 1.5 kV, *i.e.* for an interaction peer size smaller than 10nm. With such acquisition conditions and whatever the ageing time, nanoprecipitates are well-resolved, their apparent diameter is around 20nm for both ageing times, and corresponds to the sizes also measured by TEM.

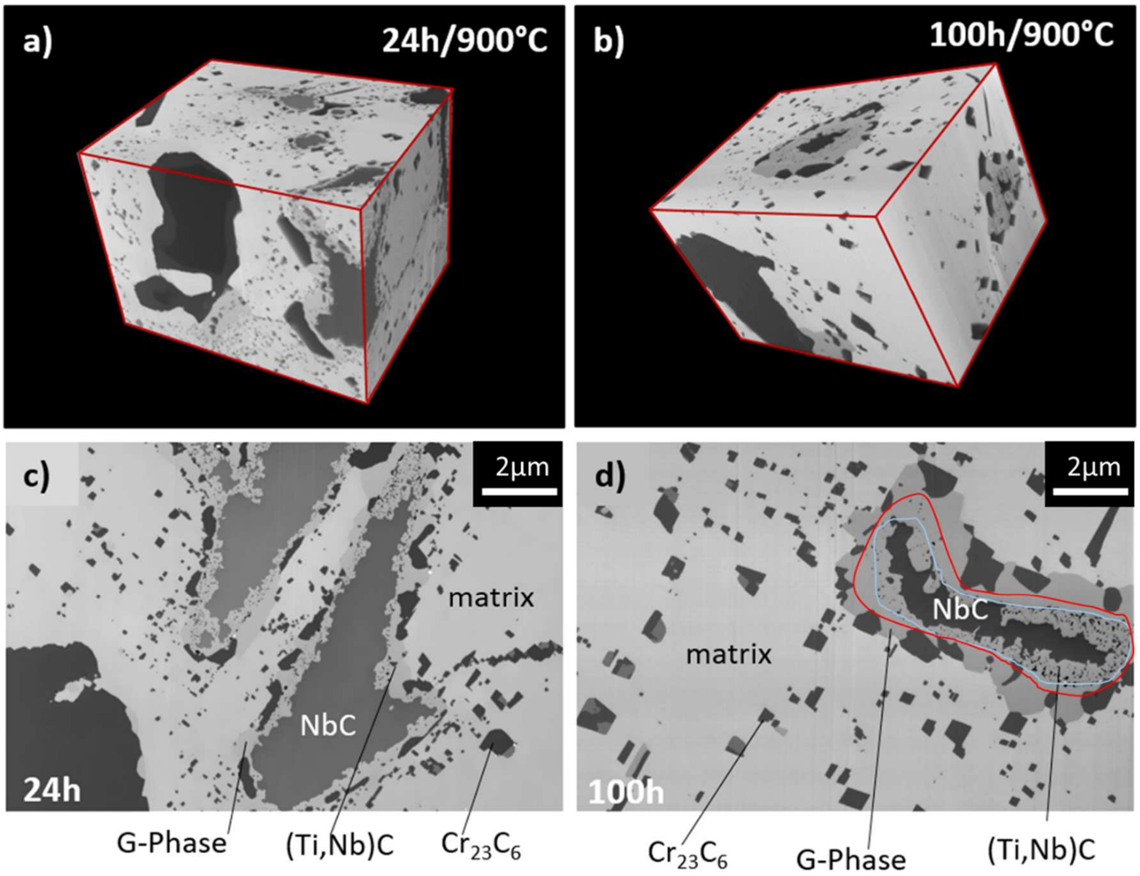

Figure 6: FIB / SEM (SE in-lens) reconstructed volumes after ageing at 900°C during 24h (a, c) and 100h (b, d) - **(a)** The volume is $9.84 \times 7.36 \times 8.00$ μm^3 and the voxel size is $(10\ nm)^3$; **(b)** The volume is $9.45 \times 6.27 \times 7.39$ μm^3 and the voxel size is $(10\ nm)^3$. **(c)** and **(d)**: slice view for both ageing times highlighting the different populations of phases: the matrix, $Cr_{23}C_6$, (Nb,Ti)C and G-phase. In red, the position of the G phase layer grown outwards and blue the position of the G phase layer gronw inwards, towards the center of the NbC.

2D sectioning of the analyzed volumes enlightens about the microstructural evolution. Upon time, the inward dissolution of the NbC precipitate, together with the simultaneous outward growth of the $Cr_{23}C_6$ and G-phase is visible (Figure 6c and d). A closer view of the Figure 6d, after 100h of ageing, reveals that the G phase layer growing at the former NbC/matrix precipitate consists of a mix layer of G phase and TiC which is assumed to be grown towards the center of the NbC (blue line) and a layer of pure G phase, which is assumed to be grown outwards (red line). One can also see that the surrounding secondary $Cr_{23}C_6$ seem larger after 100 h than after 24 h of ageing.

However, from 2D images, a quantification of the volume evolution of each phase is not possible, as the shapes are quite distorted. From the 3D volumes, a quantitative measurement of the different phase fraction evolution is possible. Indeed, as the contrasts between the different phases are quite clear, a quantitative segmentation of volumes was performed. Table 55 presents the volumes of the different extracted phases in voxel. The *G-phase$_{ext}$* refers to the G-phase growing outside the former NbC, while *G-phase$_{int}$* refers to the surrounding layer of the NbC. The former NbC (prior to transformation) is assumed to be the addition of the volumes of the transformed NbC, G-*phase$_{int}$* and the nanoparticles. In order to quantify the transformation rate of the different phases, the volume percent of each phase was calculated relatively to the volume of the untransformed NbC. After 24h, the transformation rate of NbC is 41.0%, while it is 58.5% after 100 h of ageing.

After a one-day ageing, the volume percent of *G-phase$_{ext}$* (33.3%) is close to the volume of *G-phase$_{int}$* (38.6%). However, after 100 h, the *G-phase$_{ext}$* amount has significantly increased with respect to *G-phase$_{int}$* (73.7% *vs* 54.4% respectively). This means that the NbC transformation kinetics outside the original NbC/matrix interface is faster than inside. Moreover, after 100 h of ageing, the outward growth of G-phase (73.7%) is relatively more important than that of $Cr_{23}C_6$ (59.8%), whereas after 24 h, similar volumes of both phases were formed. 3D volumes revealed that after 100 h of ageing the secondary $Cr_{23}C_6$ carbides are connected with the outward growing $Cr_{23}C_6$, which is not the case after 24 h of ageing. This might create a diffusion path for the carbon leaving the NbC precipitate. Upon time, G-phase is growing at the vicinity of the former NbC/matrix interface while $Cr_{23}C_6$ are growing further away, in the matrix.

Knowing that the relative Nb content in G-phase was estimated around 21 at% whereas it is 50at% in NbC, a release of Nb into the surrounding matrix during the transformation should be considered. Nb being a large atom, the kinetic of the internal NbC to G-phase transformation might be controlled by the release of Nb towards the matrix. Such an assumption is reinforced by the EDX line scan (Figure 4), attesting an enrichment of silicon at the matrix/NbC interface, which proves that its diffusion is not limiting here. Only niobium behaved as a limiting element, that is why we propose to estimate an effective diffusion coefficient of Nb in the G-phase at 900 °C for the investigated system.

Table 5 : Volume (in voxel) of the different segmented phases, and corresponding calculated volume % (calculated relatively to the initial NbC volume).

		G-phase int	Nanoparticles $(Ti_x,Nb_y)C$	NbC	*Calculated Former NbC ***	$M_{23}C_6$	G-phase ext
24 h	Nbr of voxels	4158656	255540	6357831	*10772027*	3522381	3588208
	volume % *	38.6	2.4	59	*100*	32.7	33.3
100 h	Nbr of voxels	11736415	873789	8952260	*21562464*	12891856	15883140
	volume % *	54.4	4.1	41.5	*100*	59.8	73.7

* relatively to the former NbC volume

** Gphase int + NbC + Nanoparticle

Discussion

To sum up, the NbC transformation at 900 °C involves two distinct mechanisms as represented in Figure 7: on one hand the inward dissolution of NbC by its transformation into a mixed continuous layer of G-phase and (Nb,Ti)C and, on the other hand, the outward simultaneous growth of $M_{23}C_6$ and G-phase. Cr_7C_3s initially present around the NbC are transformed into $Cr_{23}C_6$ during ageing, and therefore get more enriched in Cr. The rejected carbon combines with the chromium of the matrix to form secondary $Cr_{23}C_6$ precipitates. The continuous release of carbon feeds the external growth of the $Cr_{23}C_6$. Simultaneously, the initial NbC dissolves, and releases its titanium. This element cannot be incorporated into the resulting G-phase, and forms nanosized mixed (Nb,Ti)C carbides embedded into the newly formed G-phase. The inward dissolution of NbC is expected to be controlled by the Nb diffusion across the G-phase layer, as the Nb diffusion is much slower than C diffusion. The outward growth of G-phase would be controlled by the diffusion of Si from the matrix towards the Gphase/matrix interface, as the diffusion coefficient of Ni is much higher than the Si one, ($D_{Si}(M) = 1.04 \times 10^{-16} \mathrm{m}^2/s$ while $D_{Ni}(M) = 7.6 \times 10^{-15} \mathrm{m}^2/\mathrm{s}$) (LeClaire and Neumann, 1990) and as a very large amount of Ni is available in the matrix.

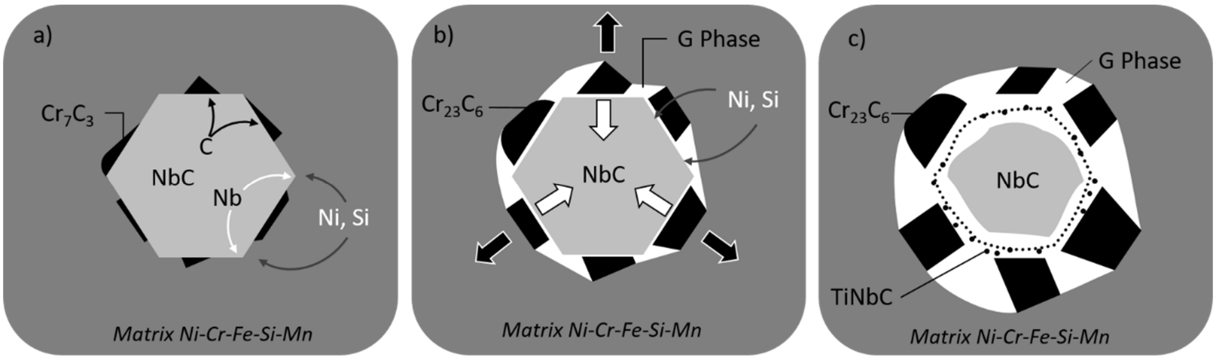

Figure 7: Schematic representation of the metallurgical transformations of NbC to G-phase.

To assess this assumption, a simple diffusion model was applied to simulate the evolution of NbC precipitates at 900 °C, and to clarify the role of Si. For a simplification purpose, the chromium carbide formation was not considered. Similarly, as mentioned before, neither the C diffusion, nor the Ni diffusion are considered as those elements are not supposed to control the growth kinetics. Only the diffusion of Si and Nb is then considered. The model is described on Figure 8. It involves a dissolving spherical NbC particle, and the formation of an external G-phase layer. This layer grows externally, moving the position of the G-phase/matrix interface towards the matrix (*r2* position on the scheme), while the dissolution of the NbC dissolution moves the NbC/G-phase interface (*r1* position) towards the center of the precipitate. The relative position of both *r1* and *r2* interfaces was determined taking into account the Nb diffusion flux at r1 interface on one hand, and the diffusion of Si at *r2* interface on the other hand.

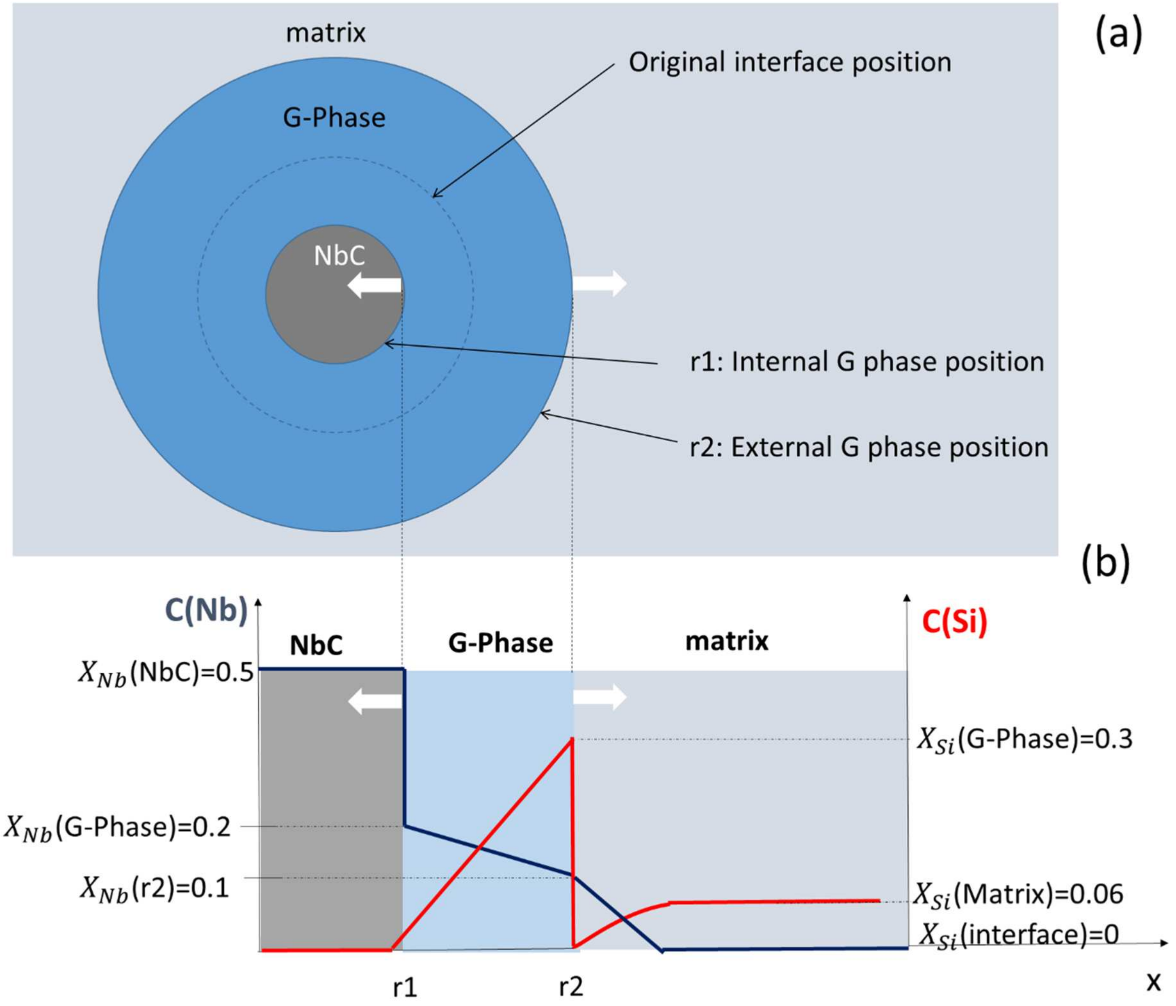

Figure 8: (a) schematic illustration of the simplified geometry of NbC precipitates adopted for the diffusion calculation at 900 °C: NbC is considered as a sphere, surrounded by an outer layer of G-phase. The NbC/G-phase interface is referred to *r1*, while the G-phase/matrix interface is denoted *r2*. (b) chemical composition profiles of Nb and Si from the center of the NbC towards the matrix. Content values (at%) are extracted from EDX measurements.

At the NbC/G-phase *r1* interface, the mass balance is given by:

$$J_{Nb}(r1).4\pi.r1^2.\delta t = 4\pi.r1^2.\delta r1.\left(X_{Nb}(G) - X_{Nb}(NbC)\right) \quad (1)$$

Therefore: $\frac{\delta r1}{\delta t} = \frac{J_{Nb}(r1)}{X_{Nb}(G) - X_{Nb}(NbC)}$

With $J_{Nb}(r1)$ the atomic diffusion flux at *r1* interface, $X_{Nb}(r1)$ the concentration of Nb at *r1* interface, and $X_{Nb}(NbC)$ the concentration of Nb in NbC.

Considering Nb contents, $X_{Nb}(NbC)$=0.5, and a gradient of Nb was experimentally observed inside the G-phase. From EDX measurements (Figure 4), we have estimated $X_{Nb}(r2)$ to 0.1 and $X_{Nb}(G)$ to 0.21.

From the first Fick's law, we have: $J_{Nb}(r1) = -D_{Nb}(G)\frac{X_{Nb}(r2)-X_{Nb}(G)}{r2-r1}$ (2)

with $D_{Nb}(G)$ the diffusion coefficient of Nb in the G-phase being an unknown parameter, to be estimated.

Combining (1) and (2) gives:

$$\frac{\delta r1}{\delta t} = -D_{Nb}(G)\frac{X_{Nb}(r2) - X_{Nb}(G)}{X_{Nb}(G) - X_{Nb}(NbC)}.\frac{1}{r2 - r1}$$

At the G-phase/matrix interface r2, a parabolic growth of the precipitate can be considered:

$$\frac{\delta r2}{\delta t} = D_{Si}(M)\frac{X_{Si}(M) - X_{Si}(r2)}{X_{Si}(G) - X_{Si}(M)}.\frac{1}{r2}$$

$with\, D_{Si}(M)$ the diffusion coefficient of Si in fcc Fe, $D_{Si}(M) = 1.04 \times 10^{-16}\mathrm{m}^2/\mathrm{s}$ and similar atomic volumes for the G-phase and the matrix.

Under those assumptions, the relative position of r1 and r2 with time was calculated, the results are plotted on Figure 9. Experimental points, derived from FIB-nt volumes, are represented as blue and red circles for the r1 and r2 values respectively. This simple model describes well the faster outward growth of the G-phase compared to the inward dissolution of the NbC. Adjusting the theoretical curves to the experimental points provides a diffusion coefficient value for Nb in G-phase of $D_{Nb}(G) = 2.5 \times 10^{-18}\mathrm{m}^2/\mathrm{s}$. This low value was expected, considering the multicomponent complex nature of the G-phase and the large size of Nb atoms.

The diffusion model describes quite well the different transformation rates that are experimentally observed for the outer G Phase/$Cr_{23}C_6$ growth and for the inward NbC dissolution. It indicates that the inward dissolution is a very long process that can explain the presence of NbC observed after thousands of hours of ageing, such as presented by Powell et al (Powell et al., 1988).

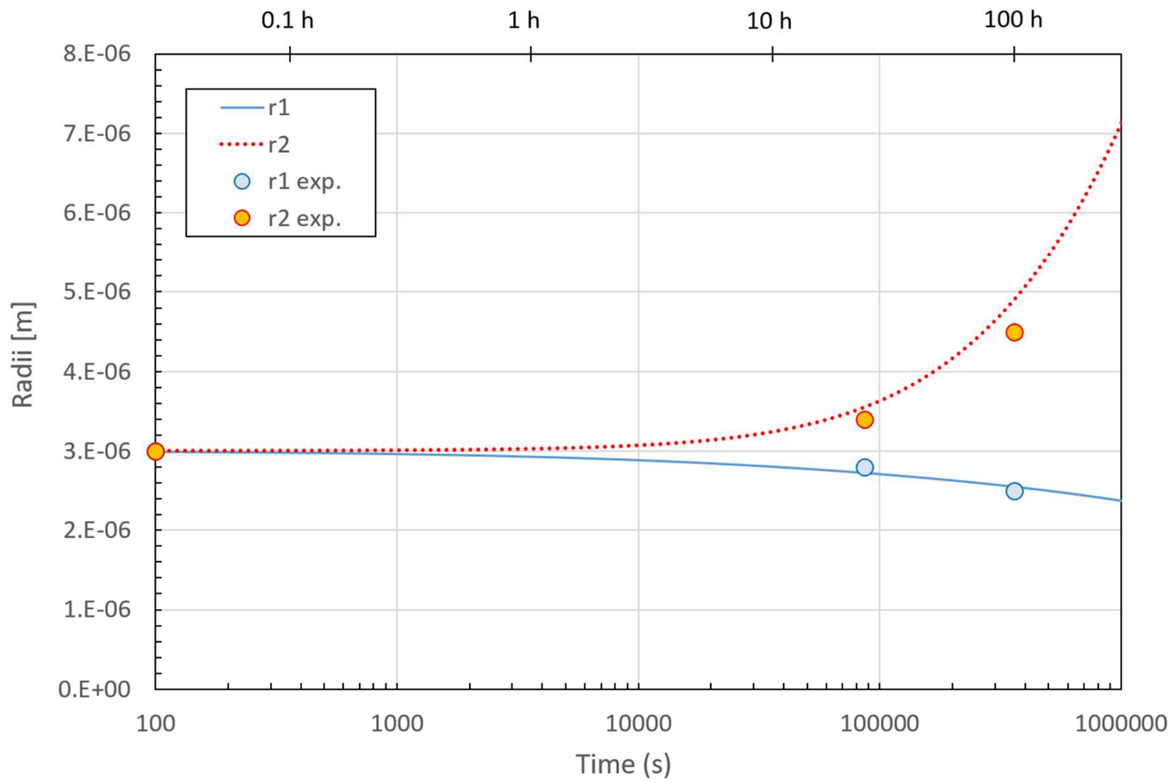

Figure 9 : Theoretical (lines) and experimental (points) evolution of the NbC/G-phase interface (*r1* in blue) and G-phase/matrix interface (*r2* in red) with time at 900 °C.

Conclusion

The microstructure of an HP alloy was investigated in the as-cast conditions and after two ageing times: 24 and 100 hours at 900 °C. A multi-scale approach, involving XRD, SEM, FiB-SEM tomography and TEM characterizations, was adopted to characterize the thermal evolution of the different phases. In its as-cast state, the alloy microstructure consists of an austenitic matrix surrounded by an interdendritic network of chromium (Cr_7C_3) and niobium (NbC) carbides. The formation of a secondary population of $Cr_{23}C_6$ precipitates, as well as the phase transformation of primary NbC carbides, were identified from the 24-hour ageing. Cr_7C_3 are completely transformed into $Cr_{23}C_6$, while the NbC to G-phase ($Ni_{16}Nb_6Si_7$) transformation is only partially achieved.

A mechanism was proposed to describe the metallurgical transformation of NbC into G-phase. A simultaneous two-step mechanism was evidenced: the inward transformation of NbC into G-phase led to a C and Nb release at the matrix/precipitate interface, which fed the growth of an external G-phase and $Cr_{23}C_6$. The diffusion of Nb through the G-phase was identified as the limiting factor for the NbC dissolution, while the diffusion of Si from the matrix towards the precipitate is controlling the outward growth of the G-phase. A value for the diffusion coefficient of Nb in the G-phase at 900 °C was calculated through a simplified model, estimated in the range of $10^{-18}\mathrm{m}^2/\mathrm{s}$.

Acknowledgments

This work was financially supported by the ANRT (Association Nationale de la Recherche et de la Technologie) through Project 2015/0205. Thanks are due to the Clym platform (www.clym.fr) for access to the FIB-SEM microscope. This research has benefited from characterization equipment of the Grenoble INP - CMTC platform supported by the Centre of Excellence of Multifunctional Architectured Materials "CEMAM" n°ANR-10-LABX-44-01 funded by the Investments for the Future programme

Declaration of interest

None

References

Andrade, A.R., Bolfarini, C., Ferreira, L.A.M., Souza Filho, C.D., Bonazzi, L.H.C., 2015. Titanium micro addition in a centrifugally cast HPNb alloy: High temperature mechanical properties. Mater. Sci. Eng. A 636, 48–52. https://doi.org/10.1016/j.msea.2015.03.085

Barbabela, G.D., de Almeida, L.H., da Silveira, T.L., Le May, I., 1991. Role of Nb in modifying the microstructure of heat-resistant cast HP steel. Mater. Charact. 26, 193–197. https://doi.org/10.1016/1044-5803(91)90053-7

Baulin, O., Douillard, T., Fabrègue, D., Perez, M., Pelletier, J.-M., Bugnet, M., 2019. Three-dimensional structure and formation mechanisms of Y2O3 hollow-precipitates in a Cu-based metallic glass. Mater. Des. 168, 107660. https://doi.org/10.1016/j.matdes.2019.107660

Berghof-Hasselbächer, E., Dechema, Materials Technology Institute of the Chemical Process Industries (U.S.),. Atlas of microstructures: AF234/7226/MSchü. Materials Technology Institute for the Chemical Process Industries, St. Louis, MO.

Buchanan, K.G., Kral, M.V., Bishop, C.M., 2014a. Crystallography and Morphology of MC Carbides in Niobium-Titanium Modified As-Cast HP Alloys. Metall. Mater. Trans. A 45, 3373–3385. https://doi.org/10.1007/s11661-014-2285-2

Buchanan, K.G., Kral, M.V., Bishop, C.M., 2014b. Crystallography and Morphology of MC Carbides in Niobium-Titanium Modified As-Cast HP Alloys. Metall. Mater. Trans. A 45, 3373–3385. https://doi.org/10.1007/s11661-014-2285-2

Burke, K.E., 1975. Chemical Extraction of refractory Inclusions from Iron- and Nickel-Base Alloy.pdf. Metallography 8, 473–488.

Buscail, H., Rolland, R., Riffard, F., Issartel, C., Combe, C., Cardey, P.-F., 2017. Influence of Sodium Hydroxide on the Austenitic 330Cb Alloy Oxidation at High Temperature. Oxid. Met. 87, 837–849. https://doi.org/10.1007/s11085-017-9722-8

de Almeida, L.H., Ribeiro, A.F., Le May, I., 2003a. Microstructural characterization of modified 25Cr–35Ni centrifugally cast steel furnace tubes. Mater. Charact. 49, 219–229. https://doi.org/10.1016/S1044-5803(03)00013-5

de Almeida, L.H., Ribeiro, A.F., Le May, I., 2003b. Microstructural characterization of modified 25Cr–35Ni centrifugally cast steel furnace tubes. Mater. Charact. 49, 219–229. https://doi.org/10.1016/S1044-5803(03)00013-5

de Almeida Soares, G.D., de Almeida, L.H., da Silveira, T.L., Le May, I., 1992. Niobium Additions in HP Heat-Resistant Cast Stainless Steels. Mater. Charact. 29, 387–392.

Dewar, M.P., Gerlich, A.P., 2013. Correlation Between Experimental and Calculated Phase Fractions in Aged 20Cr32Ni1Nb Austenitic Stainless Steels Containing Nitrogen. Metall. Mater. Trans. A 44, 627–639. https://doi.org/10.1007/s11661-012-1457-1

Ecob, R.C., Lobb, R.C., Kohler, V.L., 1987. The formation of G-phase in 20/25 Nb stainless steel AGR fuel cladding alloy and its effect on creep properties. J. Mater. Sci. 22, 2867–2880.

Guo, X.-F., Ni, Y.-Y., Gong, J.-M., Geng, L.-Y., Tang, J.-Q., Jiang, Y., Jia, X.-K., Yang, X.-Y., 2017. Formation of G-phase in 20Cr32Ni1Nb Stainless Steel and its Effect on Mechanical Properties. Acta Metall. Sin. Engl. Lett. 30, 829–839. https://doi.org/10.1007/s40195-017-0589-0

Ibañez, R.A.P., Soares, G.D.A., De Almeida, L.H., Le May, I., 1999. Effects of Si Content on the Microstructure of Modified-HP Austenitic Steels. Mater. Charact. 30, 243–249.

Joubert, J.-M., St-Fleur, W., Sarthou, J., Steckmeyer, A., Fournier, B., 2014. Equilibrium characterization and thermodynamic calculations on highly alloyed refractory steels. Calphad 46, 55–61. https://doi.org/10.1016/j.calphad.2014.02.002

Kenik, E., 2003. Structure and phase stability in a cast modified-HP austenite after long-term ageing. Scr. Mater. 49, 117–122. https://doi.org/10.1016/S1359-6462(03)00238-0

LeClaire, A.D., Neumann, G., 1990. Diffusion in Solid Metals and Alloys · Figs. 42 - 53, in: Mehrer, H. (Ed.), Diffusion in Solid Metals and Alloys Figs 42-53, Landolt-Börnstein - Group III Condensed Matter 26. Springer-Verlag Berlin Heidelberg. https://doi.org/10.1007/10390457_47

Mateo, A., Llanes, L., Anglada, M., Redjaimia, A., Metauer, G., 1997. Characterization of the intermetallic G-phase in an AISI 329 duplex stainless steel. J. Mater. Sci. 32, 4533–4540.

Mostafaei, M., Shamanian, M., Saatchi, A., Purmohamad, H., Amini, M., Mir, S.M., Shirani, A., Ezadi, J., 2009. Effect of aging temperature on structurale evolution of HP-Nb heat resistant steel. Int. J. ISSI 6, 30–33.

Nunes, F.C., de Almeida, L.H., Dille, J., Delplancke, J.-L., Le May, I., 2007. Microstructural changes caused by yttrium addition to NbTi-modified centrifugally cast HP-type stainless steels. Mater. Charact. 58, 132–142. https://doi.org/10.1016/j.matchar.2006.04.007

Pedro Ibañez, R.A., de Almeida Soares, G.D., de Almeida, L.H., Le May, I., 1993. Effects of Si content on the microstructure of modified-HP austenitic steels. Mater. Charact. 30, 243–249. https://doi.org/10.1016/1044-5803(93)90071-3

Portillo, J., Rauch, E.F., Nicolopoulos, S., Gemmi, M., Bultreys, D., 2010. Precession Electron Diffraction Assisted Orientation Mapping in the Transmission Electron Microscope. Mater. Sci. Forum 644, 1–7. https://doi.org/10.4028/www.scientific.net/MSF.644.1

Powell, D.J., Pilkington, R., Miller, D.A., 1988. The precipitation characteristics of 20% Cr25% NiNb stabilised stainless steel.pdf. Acta Metall. 36, 713–724.

Rauch, E.F., Véron, M., 2014. Automated crystal orientation and phase mapping in TEM. Mater. Charact. 98, 1–9. https://doi.org/10.1016/j.matchar.2014.08.010

Rauch, Edgar F., Véron, M., 2014. Virtual dark-field images reconstructed from electron diffraction patterns. Eur. Phys. J. Appl. Phys. 66, 10701. https://doi.org/10.1051/epjap/2014130556

Shi, F., Wang, L., Cui, W., Liu, C., 2008. Precipitation Kinetics of Cr2N in High Nitrogen Austenitic Stainless Steel. J. Iron Steel Res. Int. 15, 72–77. https://doi.org/10.1016/S1006-706X(08)60270-8

Shi, S., Lippold, J.C., 2008. Microstructure evolution during service exposure of two cast, heat-resisting stainless steels — HP–Nb modified and 20–32Nb. Mater. Charact. 59, 1029–1040. https://doi.org/10.1016/j.matchar.2007.08.029

Sourmail, T., 2001. Precipitation in creep resistant austenitic stainless steels. Mater. Sci. Technol. 17, 1–14.

Sustaita-Torres, I.A., Haro-Rodríguez, S., Guerrero-Mata, M.P., de la Garza, M., Valdés, E., Deschaux-Beaume, F., Colás, R., 2012a. Aging of a cast 35Cr–45Ni heat resistant alloy. Mater. Chem. Phys. 133, 1018–1023. https://doi.org/10.1016/j.matchemphys.2012.02.010

Sustaita-Torres, I.A., Haro-Rodríguez, S., Guerrero-Mata, M.P., de la Garza, M., Valdés, E., Deschaux-Beaume, F., Colás, R., 2012b. Aging of a cast 35Cr–45Ni heat resistant alloy. Mater. Chem. Phys. 133, 1018–1023. https://doi.org/10.1016/j.matchemphys.2012.02.010

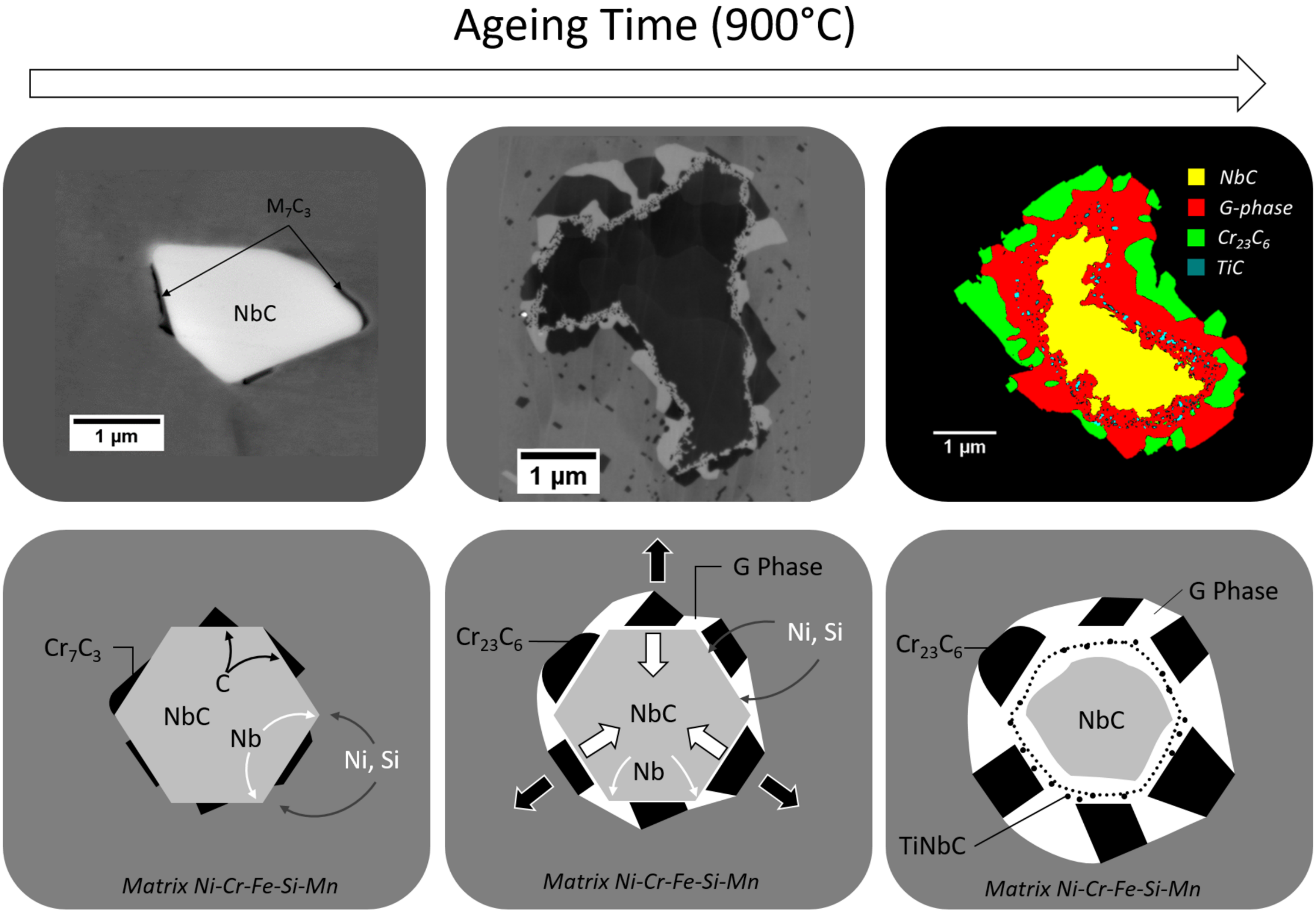
Ageing Time (900°C)
M7C3
NbC
1 µm
1 µm
NbC
G-phase
Cr23C6
TiC
1 µm
Cr7C3
C
NbC
Nb
Ni, Si
Matrix Ni-Cr-Fe-Si-Mn
G Phase
Cr23C6
Ni, Si
NbC
Nb
Matrix Ni-Cr-Fe-Si-Mn
G Phase
Cr23C6
NbC
TiNbC
Matrix Ni-Cr-Fe-Si-Mn